Monthly Notices of the ROYAL ASTRONOMICAL SOCIETY

MNRAS **527,** 731–738 (2024) https://doi.org/10.1093/mnras/stad3226
Advance Access publication 2023 October 21

ExoMol line lists – LI. Molecular line lists for lithium hydroxide (LiOH)

Alec Owens [1]★ Sam O. M. Wright,[1] Yakiv Pavlenko,[2,3] Alexander Mitrushchenkov,[4] Jacek Koput [5] Sergei N. Yurchenko [1]★ and Jonathan Tennyson [1]★

[1]*Department of Physics and Astronomy, University College London, Gower Street, London WC1E 6BT, UK*
[2]*Instituto de Astrofísica de Canarias (IAC), Calle Vía Láctea s/n, E-38200 La Laguna, Tenerife, Spain*
[3]*Main Astronomical Observatory, Academy of Sciences of the Ukraine, 27 Zabolotnoho, UA-03143 Kyiv, Ukraine*
[4]*MSME, Université Gustave Eiffel, CNRS UMR 8208, Univ Paris Est Creteil, F-77474 Marne-la-Vallée, France*
[5]*Department of Chemistry, Adam Mickiewicz University, PL-61-614 Poznan, Poland*

Accepted 2023 October 17. Received 2023 October 17; in original form 2023 July 25

ABSTRACT

New molecular line lists for lithium hydroxide (^{6}Li^{16}O^{1}H and ^{7}Li^{16}O^{1}H isotopologues) covering wavelengths $\lambda > 1$ μm (0–10 000 cm^{-1} range) are presented. Each line list contains around 300 million transitions between rotation–vibration energy levels with total angular momentum up to $J = 95$, applicable for temperatures up to $T \approx 3500$ K. Line list calculations were based on a previously published, high-level *ab initio* potential energy surface and a newly computed dipole moment surface of the ground $\tilde{X}\,^1\Sigma^+$ electronic state. Lithium-containing molecules are important in a variety of stellar objects and there is potential for LiOH to be observed in the atmospheres of exoplanets. Transit spectra are simulated using the rocky super-Earth 55 Cancri e as an example with two different atmospheric scenarios including LiOH. This work provides the first, comprehensive line lists of LiOH to facilitate its future molecular detection. The OYT7 line lists along with the associated temperature- and pressure-dependent molecular opacities can be downloaded from the ExoMol database at www.exomol.com and the CDS astronomical database.

Key words: molecular data – opacity – planets and satellites: atmospheres – stars: atmospheres – ISM: molecules.

1 INTRODUCTION

Ultracool dwarfs occupy the right-bottom corner of the Hertzsprung–Russell diagram. The rates of depletion of lithium (and deuterium) in their interiors are primarily determined by the mass of the star or substellar object. For stars with $M > 85M_J$, the burning of lithium, Li (p, α) ^{4}He, becomes efficient at early evolutionary stages preceding the main sequence at interior temperatures of $T \sim 2.5$ MK (D'Antona & Mazzitelli 1998). Young, low-mass stars possess developed convective envelopes, so lithium depletion in their central region occurs on relatively short time-scales (several tens of millions of years), resulting in a weakening or complete disappearance of lithium lines in their spectra. The temperature in the interior of brown dwarfs with masses less than $60M_J$ is not high enough for lithium burning. Thus, in principle, their primordial lithium abundance should not change with time. This circumstance led to the idea of the lithium test (Rebolo, Martin & Magazzu 1992), which essentially equates to searching for lithium absorption lines in the spectra of ultracool dwarfs as evidence of their substellar nature.

The lithium abundance in the atmosphere of young stellar objects is of special interest. In particular, the position of the line in the Hertzsprung–Russell diagram separating stars burning lithium from lower mass objects with lithium still in their atmospheres can be used to derive independent age estimates for young open clusters less than 150 Myr in age (D'Antona & Mazzitelli 1998). Pavlenko et al. (1995) showed that despite strong blending and formation of lithium-containing molecules, observation of Li resonance doublets is possible in M-dwarfs despite the strong presence of TiO and VO. Indeed, Rebolo et al. (1996) observed Li resonance doublets in the spectrum of the first brown dwarf Teide 1 and rather high lithium abundance $\log N(\mathrm{Li}) = 3.2 \pm 0.2$ (Pavlenko 1997). The lithium test was successfully used to prove the substellar nature of several late-type dwarfs of spectral class M (Ruiz, Leggett & Allard 1997; Zapatero Osorio et al. 2002).

In the case of late L- and T-dwarfs, the numerous molecular lithium-containing species bind most of the Li atoms (Tsuji 1973). Li I is not a dominant species. Recent observations suggest that Li I has been found in L- and T-dwarfs down to a spectral type as cool as T3.5 (Martín, Lodieu & del Burgo 2021). However, lithium hydroxide (main isotopologue ^{7}Li^{16}O^{1}H; referred to as LiOH from here on in) is one of the most abundant molecules, along with LiF and LiCl (Pavlenko, Zapatero Osorio & Rebolo 2000). We note that line lists for LiF and LiCl were created by Bittner & Bernath (2018) as part of the MoLLIST project (Bernath 2020) and are also available from the ExoMol database (Tennyson et al. 2020). The isotope ^{6}Li is less abundant with the solar lithium isotopic ratio ^{7}Li/^{6}Li being only 12.175 (Lodders, Palme & Gail 2009). However, the search and analysis of ^{6}LiOH is of great interest in the atmosphere of ultracool subdwarfs, which should preserve both ^{6}Li and ^{7}Li from the early epochs of our Galaxy's evolution. For cooler T- and Y- dwarfs, the maximum of the spectral energy distribution shifts towards the infrared (IR) and fluxes in the optical spectral range become

★ E-mail: alec.owens.13@ucl.ac.uk (AO); s.yurchenko@ucl.ac.uk (SNY); j.tennyson@ucl.ac.uk (JT)

extremely weak. Moreover, due to the lower temperatures, lithium presumably exists in the form of molecules. Thus, the computation of spectral features formed by lithium-containing species such as LiOH is the only way to determine the lithium abundance in cooler atmospheres (Gharib-Nezhad et al. 2021).

There is very limited knowledge of the gas-phase rotation–vibration (rovibrational) spectrum of lithium hydroxide. Pure rotational transitions in the ground vibrational state and excited ν_2 bending vibrational states have been measured (McNaughton et al. 1994; Higgins et al. 2004), confirming the linear equilibrium geometry of LiOH. Gurvich et al. (1996) reviewed the available data on thermodynamic and molecular properties of gas-phase LiOH, highlighting the lack of experimental studies. Theoretical calculations have been carried out using full-dimensional *ab initio* potential energy surfaces (PESs; Bunker et al. 1989; Higgins et al. 2004; Koput 2013) providing key insight into the rovibrational energy level structure; however, without essential information on the strength of transition intensities, the chances of observing this molecule in astronomical environments is limited. To this end, we present newly computed molecular line lists of ^{6}Li^{16}O^{1}H and ^{7}Li^{16}O^{1}H covering IR wavelengths $\lambda > 1$ μm (0–10 000 cm^{-1}). The new line lists, named OYT7, are available from the ExoMol database (Tennyson & Yurchenko 2012; Tennyson et al. 2016, 2020), which is providing comprehensive molecular data to aid the atmospheric modelling of exoplanets and other hot astronomical bodies. In the Solar system, lithium abundance is composed of two stable isotopes ^{7}Li and ^{6}Li with approximately 92.4 and 7.6 per cent abundance.

The paper is structured as follows: In Section 2, we describe the computational set-up and theoretical spectroscopic model used to generate the LiOH line lists. Results are discussed in Section 3, where we detail the structure and format of the line list along with generated opacities, analyse the temperature-dependent partition function, and simulate spectra of LiOH with a focus on potential detection in exoplanet atmospheres. Conclusions are offered in Section 4.

2 METHODS

The computational procedure for generating molecular line lists is well established (Tennyson 2016; Tennyson & Yurchenko 2017) with numerous line lists having been produced for the ExoMol database. Calculations require molecular PESs, dipole moment surfaces (DMSs), and a variational nuclear motion program to solve the Schrödinger equation to obtain rovibrational energy levels and all possible transition probabilities between them.

2.1 Potential energy surface

We utilize a previously published *ab initio* PES of the $\tilde{X}\,^1\Sigma^+$ electronic ground state of LiOH (Koput 2013). The PES was computed using coupled cluster methods in conjunction with a large augmented correlation-consistent basis set [CCSD(T)/aug-cc-pCV6Z level of theory] and treated a range of higher level additive energy corrections. These included core–valence electron correlation, higher order coupled cluster terms beyond perturbative triples, scalar relativistic effects, and the diagonal Born–Oppenheimer correction. Computing the PES with a composite approach like this can be very accurate, predicting fundamental vibrational wavenumbers to within 1 cm^{-1} accuracy on average. For ^{7}LiOH, the fundamental vibrational wavenumbers are predicted to be $\nu_1 = 925.37$ cm^{-1} for the Li–O stretching mode, $\nu_2 = 319.49$ cm^{-1} for the Li–O–H bending mode, and $\nu_3 = 3833.14$ cm^{-1} for the O–H stretching mode. Since no gas-phase vibrational spectra of LiOH have been measured, it is not possible to confirm this level of accuracy. However, other molecular *ab initio* PESs constructed in a similar manner have consistently achieved sub-wavenumber accuracy for the fundamentals and many other vibrational levels (Owens et al. 2015a, b, 2016).

The PES was represented as a 10th-order polynomial expansion of the form

$$V = \sum_{ijk} f_{ijk} \xi_1^i \xi_2^j \xi_3^k, \tag{1}$$

with the vibrational coordinates,

$$\xi_1 = (r_1 - r_1^{\rm eq})/r_1, \tag{2}$$

$$\xi_2 = (r_2 - r_2^{\rm eq})/r_2, \tag{3}$$

$$\xi_3 = \alpha - \alpha_{\rm eq}. \tag{4}$$

Here, the stretching coordinates $r_1 = r_{\rm LiO}$, $r_2 = r_{\rm OH}$, the interbond angle $\alpha = \angle$(LiOH), the equilibrium parameters are $r_1^{\rm eq}$, $r_2^{\rm eq}$, and $\alpha_{\rm eq}$, and f_{ijk} are the expansion parameters (44 in total; see table IV of Koput 2013 for values). The PES of LiOH is provided as supplementary material.

2.2 Dipole moment surface

A new DMS of LiOH in the $\tilde{X}\,^1\Sigma^+$ ground state was computed using the coupled cluster singles and doubles with perturbative triples CCSD(T) method in conjunction with the correlation-consistent basis sets aug-cc-pCVQZ for Li (Prascher et al. 2011) and O (Woon & Dunning 1995), and aug-cc-pVQZ for H (Kendall, Dunning & Harrison 1992). Calculations used the quantum chemical program MOLPRO2015 (Werner et al. 2012, 2020) and were carried out on the same grid of nuclear geometries used to compute the PES, namely 274 points in the range $1.20 \leq r_{\rm LiO} \leq 2.40$ and $0.75 \leq r_{\rm OH} \leq 1.30$ for the stretches, and $60.0^\circ \leq \alpha_{\rm LiOH} \leq 180.0^\circ$ for the bending motion.

The instantaneous dipole moment vector $\boldsymbol{\mu}$ was represented in the pq axis system (Jørgensen & Jensen 1993). In this representation, the origin is fixed at the O nucleus with the p and q axes defined in the plane of the three nuclei. The q axis bisects the interbond angle $\alpha = \angle$(LiOH), while the p axis lies perpendicular to the q axis, e.g. at linearity the p axis is along the molecular bond with the Li nucleus in the positive direction. In DMS calculations, the dipole moment components μ_p and μ_q were determined via central finite differences by applying an external electric field with components ±0.005 au along the p and q axes, respectively.

Once computed, the μ_p and μ_q components were represented analytically using the expressions

$$\mu_p = \sum_{ijk} F_{ijk}^{(p)} \zeta_1^i \zeta_2^j \zeta_3^k \tag{5}$$

and

$$\mu_q = \sin(\pi - \alpha) \sum_{ijk} F_{ijk}^{(q)} \zeta_1^i \zeta_2^j \zeta_3^k. \tag{6}$$

Here, the vibrational coordinates are

$$\zeta_1 = r_1 - r_1^{\rm eq}, \tag{7}$$

$$\zeta_2 = r_2 - r_2^{\rm eq}, \tag{8}$$

$$\zeta_3 = \cos\alpha - \cos\alpha_{\rm eq}, \tag{9}$$

with values of $r_1^{\rm eq} = 1.6000$ Å, $r_2^{\rm eq} = 0.9478$ Å, and $\alpha_{\rm eq} = 180.0^\circ$. A sixth-order expansion ($i + j + k = 6$) was used to determine the

Table 1. Extract from the `.states` file of the ^{7}LiOH OYT7 line list.

i	$\tilde{E}$ (cm^{-1})	g_i	J	unc	τ	e/f	State	v_1	v_2	L_2	v_3
1	0.000 000	8	0	0.000 000	1	e	X(1SIGMA+)	0	0	0	0
2	610.710 042	8	0	4.000 000	1	e	X(1SIGMA+)	0	2	0	0
3	925.369 014	8	0	2.000 000	1	e	X(1SIGMA+)	1	0	0	0
4	1214.983 732	8	0	8.000 000	1	e	X(1SIGMA+)	0	4	0	0
5	1514.667 551	8	0	6.000 000	1	e	X(1SIGMA+)	1	2	0	0

Notes. i: state counting number; $\tilde{E}$: state energy (in cm^{-1}); g_i: total statistical weight, equal to $g_{\rm ns}(2J+1)$; J: total angular momentum; unc: uncertainty (in cm^{-1}); τ: total parity; e/f: rotationless parity; State: electronic state $X^1\Sigma^+$; v_1: symmetric stretching ν_1 mode vibrational quantum number; v_2: bending ν_2 mode vibrational quantum number; L_2: vibrational angular momentum quantum number $L_2 = |l_2|$ associated with ν_2 mode; v_3: antisymmetric stretching ν_3 mode vibrational quantum number.

Table 2. Extract from the `.trans` file of the ^{7}LiOH OYT7 line list.

f	i	A_{fi}
150 641	153 947	4.495 848 94E−02
169 519	168 283	1.916 541 38E−01
192 086	190 852	4.316 289 48E−02
3950	5918	4.147 300 97E−09
61 456	62 578	7.304 436 03E−06

Notes. f: upper state counting number; i: lower state counting number; A_{fi}: Einstein A coefficient (in s^{-1}).

expansion parameters $F_{ijk}^{(p/q)}$ in a least-squares fitting to the *ab initio* data utilizing Watson's robust fitting scheme (Watson 2003). The μ_p component was fitted with 72 parameters (excluding equilibrium parameters) and reproduced the *ab initio* data with a root-mean-square (rms) error of 1.2×10^{-4} Debye. For the μ_q component, 64 parameters achieved an rms error of 6.5×10^{-6} Debye in the fitting. The DMS of LiOH is provided as supplementary material.

2.3 Line list calculations

Line list calculations employed the computer program EVEREST (Mitrushchenkov 2012), which was previously used to generate a rotation–vibration–electronic line list of the linear triatomic molecule CaOH (Owens et al. 2022) for the ExoMol database. We provide a summary of the key calculation parameters and steps since a full description of the methodology used by EVEREST can be found in Mitrushchenkov (2012).

Valence bond length–bond angle coordinates were employed with a discrete variable representation (DVR) basis consisting of 100 Sinc-DVR functions on both the Li–O bond in the 2.0–7.0a_0 interval and the O–H bond in the 1.1–6.0a_0 interval, and 120 Legendre functions for the ∠(LiOH) bond angle in the range 0.0–180.0°. Vibrational eigenfunctions up to 10 000 cm^{-1} above the $\tilde{X}\,^1\Sigma^+$ ground state were computed from a Hamiltonian of dimension 10 000 for $0 \leq K \leq 20$, where $K = |\Lambda + l|$ (Λ and l are the projections of the electronic and vibrational angular momenta along the linear axis, respectively). The full rotation–vibration (rovibrational) Hamiltonian was diagonalized using the vibrational eigenfunctions for values of J up to 95, where J is the total angular momentum quantum number. Above $J = 95$, the lowest rovibrational energy level lies above 10 000 cm^{-1} and beyond the intended accuracy of the underlying PES (Koput 2013). Intensities to these high-lying rovibrational states will be extremely weak. However, we did not want to extrapolate too substantially in our calculations, so employed $J = 95$ as an upper limit. This corresponds to the maximal temperature of the line list of 3500 K estimated via the convergence of the partition function $Q(T)$ as discussed in Section 3.3. Convergence of the computed rovibrational energy levels was tested by increasing the Hamiltonian dimension, setting $K \leq 30$, extending the DVR grids of the coordinates and increasing the number of basis functions.

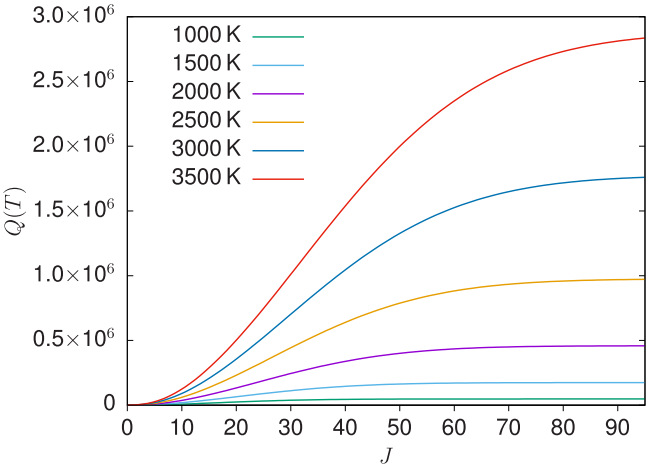

Figure 1. Convergence of the temperature-dependent partition function $Q(T)$ of ^{7}Li^{16}O^{1}H with respect to the total angular momentum quantum number J at various temperatures (in K).Al

Atomic mass values were used in EVEREST calculations with values of 7.014 357 696 863 Da (^{7}Li), 6.013 477 147 693 Da (^{6}Li), 15.990 525 980 297 Da (O), and 1.007 276 452 321 Da (H) (Wang et al. 2012). The zero-point energies of ^{7}LiOH and ^{6}LiOH were computed to be 2780.676 and 2808.347 cm^{-1}, respectively. Rovibrational energy levels, transitions, and Einstein A coefficients were computed for the $\tilde{X}\,^1\Sigma^+$ ground state covering the 0–10 000 cm^{-1} range (wavelengths $\lambda > 1$ μm). The final LiOH line lists contained 331 274 717 transitions between 203 762 states for ^{7}LiOH, and 294 573 305 transitions between 192 412 states for ^{6}LiOH with total angular momentum up to $J = 95$.

3 RESULTS

3.1 Line list format

As standard, the ExoMol data format (Tennyson et al. 2020) was used to represent each line list as two file types. The `.states` file, an example of which is given in Table 1, lists all the computed rovibrational energy levels (in cm^{-1}), a value for the uncertainty (in cm^{-1}), and quantum numbers from the EVEREST calculations to

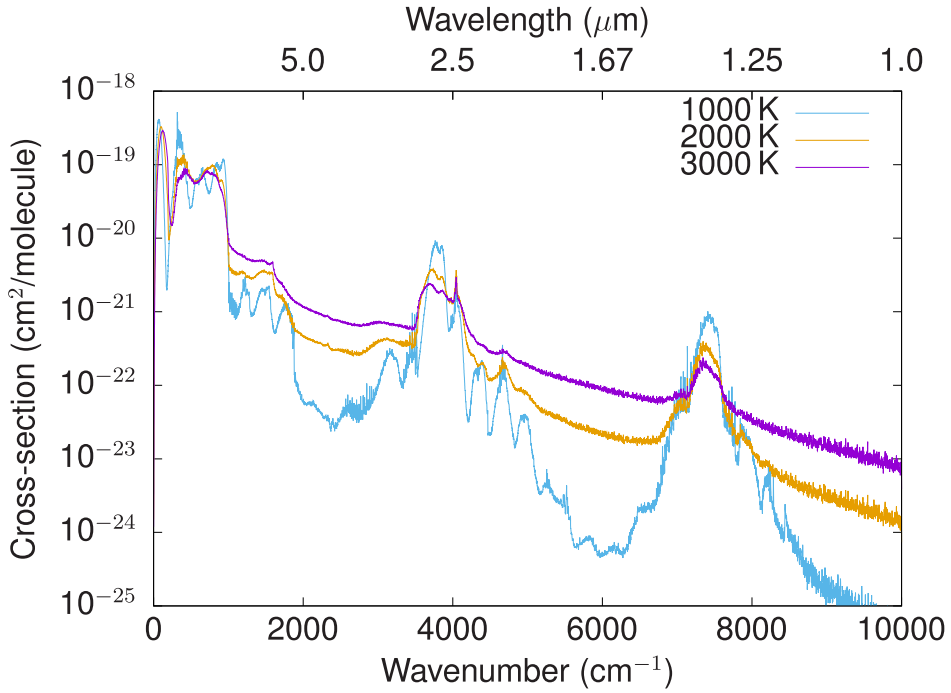

Figure 2. Temperature-dependent spectra of ^{7}Li^{16}O^{1}H. Absorption cross-sections were computed at a resolution of 1 cm^{-1} and modelled with a Gaussian line profile with an HWHM of 1 cm^{-1} for high temperatures (in K).

identify the states. The `.trans` file, as seen in Table 2, lists the computed transitions via upper and lower state ID running numbers, and Einstein *A* coefficients (in s^{-1}).

The uncertainties of the energy levels have been estimated as 2 cm^{-1} for the fundamental vibrational states. For excited vibrational states, the uncertainty has been cumulatively added from the contributions of the fundamentals, e.g. the state $4\nu_1 + \nu_2$ has an uncertainty of 10 cm^{-1}. These estimates are conservative and are based on the *ab initio* approach used to generate the PES of LiOH (Koput 2013). We expect the energies to be more accurate; however, we want to ensure that all users are aware that the LiOH line list is based on theoretical predictions and has not been refined to experimental data. A number of line lists in the ExoMol database have been, or are currently being, adapted for high-resolution applications, namely the high-resolution spectroscopy of exoplanets (Snellen 2014; Birkby 2018). This is only possible when there are extensive laboratory measurements to replace the computed energy levels by empirically derived values using the MARVEL (measured active vibration-rotation energy levels) procedure (Császár et al. 2007; Furtenbacher, Császár & Tennyson 2007; Furtenbacher & Császár 2012; Tóbiás et al. 2019), which is not possible for LiOH due to the lack of experimental data. In any case, the LiOH line lists should be accurate enough for low-resolution transit studies of exoplanetary atmospheres, and for stellar atmospheric modelling; the shapes of the corresponding bands and intensities should be of sufficient quality.

The vibrational quantum number labelling of the energy levels was determined in EVEREST by assigning values based on the underlying basis functions used in the variational nuclear motion calculations. The assignments are usually very reliable at lower energies and excitation, but become more approximate for highly excited vibrational states, where mixing between the different molecular motions comes into effect. The vibrational quantum numbers used are v_1 (symmetric stretching ν_1 mode vibrational quantum number), v_2 (bending ν_2 mode vibrational quantum number), l_2 vibrational angular momentum quantum number associated with the ν_2 mode, and v_3 (antisymmetric stretching ν_3 mode vibrational quantum number).

3.2 ExoMolOP opacities of LiOH

Temperature- and pressure-dependent molecular opacities of LiOH based on the OYT7 line lists have been generated for four exoplanet atmospheric retrieval codes ARCIS (Min et al. 2020), TAUREX (Al-Refaie et al. 2021), NEMESIS (Irwin et al. 2008), and PETITRADTRANS (Molliére et al. 2019) using the ExoMolOP procedure (Chubb et al. 2021). The ExoMolOP temperature grid consisted of 27 values [100, 200, 300, 400, 500, 600, 700, 800, 900, 1000, 1100, 1200, 1300, 1400, 1500, 1600, 1700, 1800, 1900, 2000, 2200, 2400, 2600, 2800, 3000, 3200, 3400] K; the pressure grid used was [1×10^{-5}, $2.154\,434\,69 \times 10^{-5}$, $4.641\,588\,83 \times 10^{-5}$, 1×10^{-4}, $2.154\,434\,69 \times 10^{-4}$, $4.641\,588\,83 \times 10^{-4}$, 1×10^{-3}, $2.154\,434\,69 \times 10^{-3}$, $4.641\,588\,83 \times 10^{-3}$, 1×10^{-2}, $2.154\,434\,69 \times 10^{-2}$, $4.641\,588\,83 \times 10^{-2}$, 1×10^{-1}, $\times 10^{-1}$, $4.641\,588\,83 \times 10^{-1}$, 1, 2.154 434 69, 4.641 588 83, 10, 21.544 3469, 46.415 8883, 100] bar. In total, three sets of LiOH opacities were computed: (i) the opacity of ^{6}Li^{16}O^{1}H, (ii) the opacity of ^{7}Li^{16}O^{1}H, and (iii) the combined opacity of ^{6}Li^{16}O^{1}H and ^{6}Li^{16}O^{1}H using the solar abundance ratio 0.759:0.9241. For the line broadening, we assumed an 85 per cent H_2 and 15 per cent He atmosphere and Voigt line profile with the following parameters: $\gamma_{H_2} = 0.12$ cm^{-1}, $n_{H_2} = 0.5$, $\gamma_{He} = 0.05$ cm^{-1}, and $n_{He} = 0.5$.

3.3 Temperature-dependent partition function

The temperature-dependent partition function $Q(T)$ for each isotopologue of LiOH has been calculated on a 1 K grid in the 1–4000 K range and is provided alongside the LiOH line lists from the ExoMol

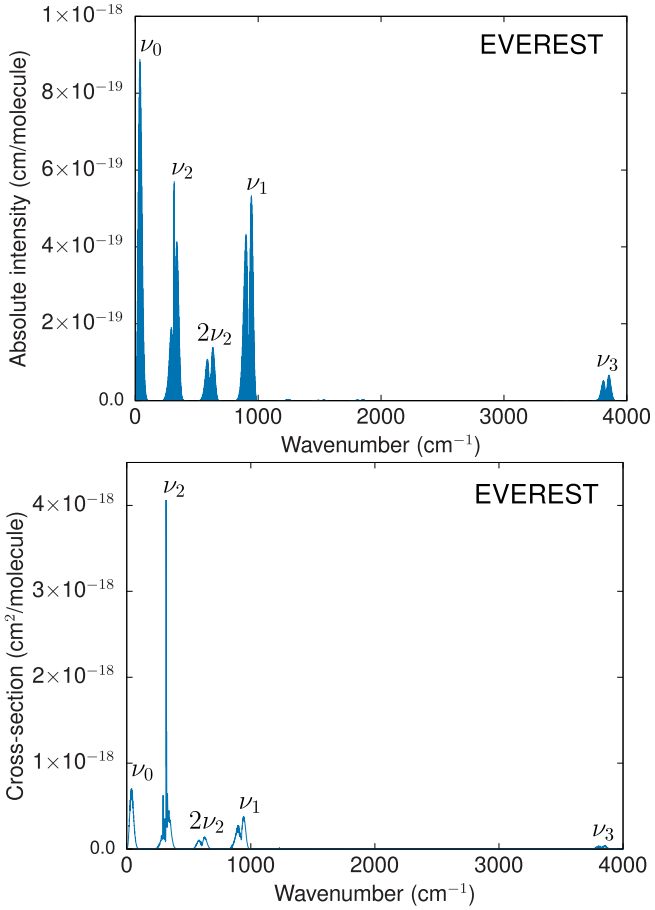

Figure 3. Comparison of computed absolute line intensities (upper panel) and absorption cross-sections (lower panel) of ^{7}Li^{16}O^{1}H at $T = 300$ K. The pure rotational band (ν_0), Li–O stretching band (ν_1), Li–O–H bending band (ν_2), O–H stretching band (ν_3), and the bending overtone band ($2\nu_2$) are labelled.

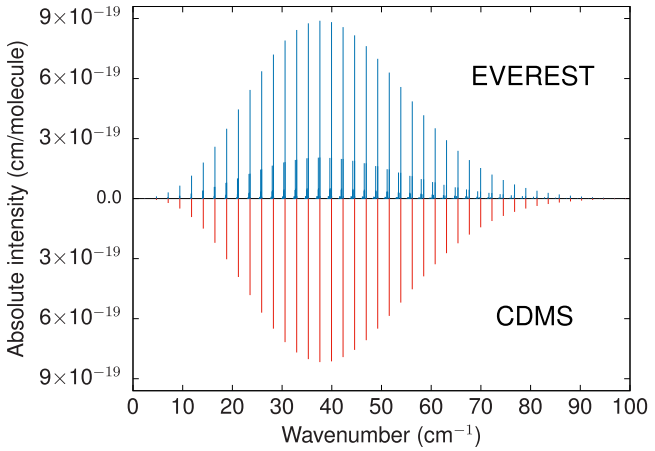

Figure 4. Computed stick spectrum of ^{7}Li^{16}O^{1}H at $T = 300$ K (not scaled to natural abundance) in the microwave region compared against all transition data from the CDMS (Müller et al. 2001, 2005).

website. Values were obtained by summing over all of the computed rovibrational energy levels using the expression

$$Q(T) = \sum_i g_i \exp\left(\frac{-E_i}{kT}\right), \tag{10}$$

where $g_i = g_{\rm ns}(2J_i + 1)$ is the degeneracy of a state i with energy E_i and total angular momentum quantum number J_i, and the nuclear spin statistical weight $g_{\rm ns} = 8$ for ^{7}Li^{16}O^{1}H, and $g_{\rm ns} = 6$ for ^{6}Li^{16}O^{1}H.

In Fig. 1, the convergence of $Q(T)$ of ^{7}LiOH as a function of J is illustrated for different temperatures, essentially showing how more energy levels have to be included in the summation at higher temperatures to achieve converged values. The curve for $T = 3500$ K at higher J does not plateau, meaning $Q(T)$ is not fully converged, and we therefore recommend this temperature as a soft upper limit for using the LiOH line lists. Using the line lists above this temperature will lead to a progressive loss of opacity, so caution must be exercised if doing so.

At $T = 300$ K, we compute the partition function of ^{7}Li^{16}O^{1}H to be $Q = 2360.22$. This is much larger than the value available from the Cologne Database for Molecular Spectroscopy (CDMS; Müller et al. 2001, 2005), which gives $Q_{\rm CDMS} = 1420.69$ (including the contribution from $g_{\rm ns} = 8$). This discrepancy can be attributed to the fact that the value from CDMS only considers the ground vibrational state. However, in LiOH, there are low-lying rovibrational states that should be properly accounted for. To check this, a partition function value of $Q = 1427.80$ was determined from the OYT7 line list by only including contributions from the ground vibrational state in the summation of equation (10). This comparison highlights the importance of treating rovibrational states in the calculation of the temperature-dependent partition function.

3.4 Simulated spectra

An overview of the spectrum of ^{7}Li^{16}O^{1}H is shown in Fig. 2, where we have simulated temperature-dependent absorption cross-sections at high temperatures. Cross-sections were calculated at a resolution of 1 cm^{-1} and modelled with a Gaussian line profile with a half width at half maximum (HWHM) of 1 cm^{-1}. Calculations used the EXOCROSS program (Yurchenko, Al-Refaie & Tennyson 2018), which is based on the methodology presented in Hill, Yurchenko & Tennyson (2013). As evident in Fig. 2, increasing the temperature causes the rotational bands to broaden substantially, a result of the increased population in vibrationally excited states, leading to much flatter and smoother spectral features. Note that zero-pressure cross-sections of LiOH can be obtained using the ExoMol cross-sections app at www.exomol.com for any temperature between 100 and 5000 K (see Hill et al. 2013).

The strongest features occur at longer wavelengths where the rotational and fundamental bands lie. In Fig. 3 (upper panel), we have plotted absolute line intensities (in units of cm per molecule) at $T = 300$ K showing these bands. Line intensities were computed as

$$I(f \leftarrow i) = \frac{A_{fi}}{8\pi c} g_{\rm ns}(2J_f + 1) \frac{\exp(-E_i/kT)}{Q(T)\,\nu_{fi}^2} \times \left[1 - \exp\left(-\frac{hc\nu_{fi}}{kT}\right)\right], \tag{11}$$

where A_{fi} is the Einstein A coefficient of a transition with wavenumber ν_{fi} (in cm^{-1}) between an initial state with energy E_i and a final state with rotational quantum number J_f. Here, k is the Boltzmann constant, h is the Planck constant, c is the speed of light, T is the absolute temperature, $Q(T)$ is the partition function, and the nuclear

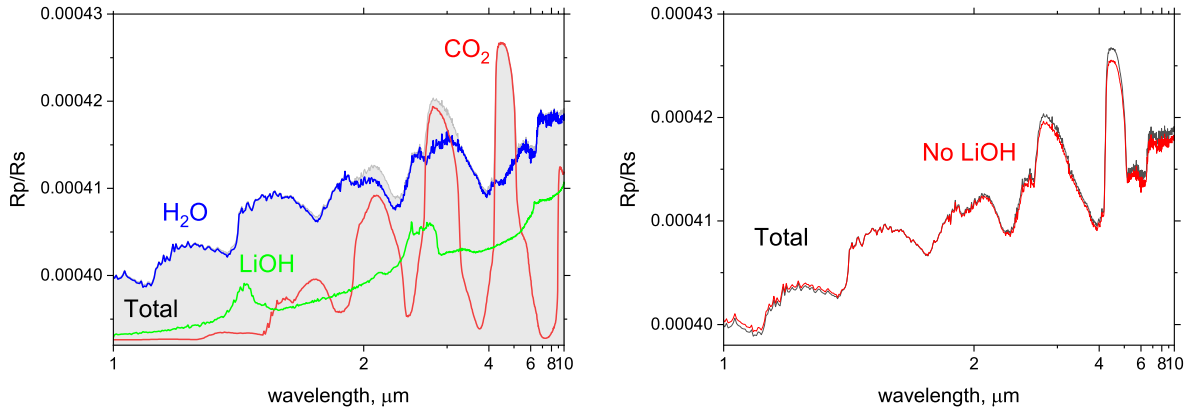

Figure 5. A simulated transit spectrum of an atmosphere with 45 per cent of CO_2, 45 per cent of water, and 5 per cent LiOH using the TAUREX-III radiative transfer code (Al-Refaie et al. 2021) showing how water masks the strongest OH stretching bands of LiOH. The left display shows individual contributions as different colour lines as well as the total spectrum (grey area). The right display compares the total spectrum (black) and a spectrum where the LiOH contribution was excluded (red). An offset of +0.000 000 796 959 was applied in order to make the effect of including LiOH into the opacity more clear.

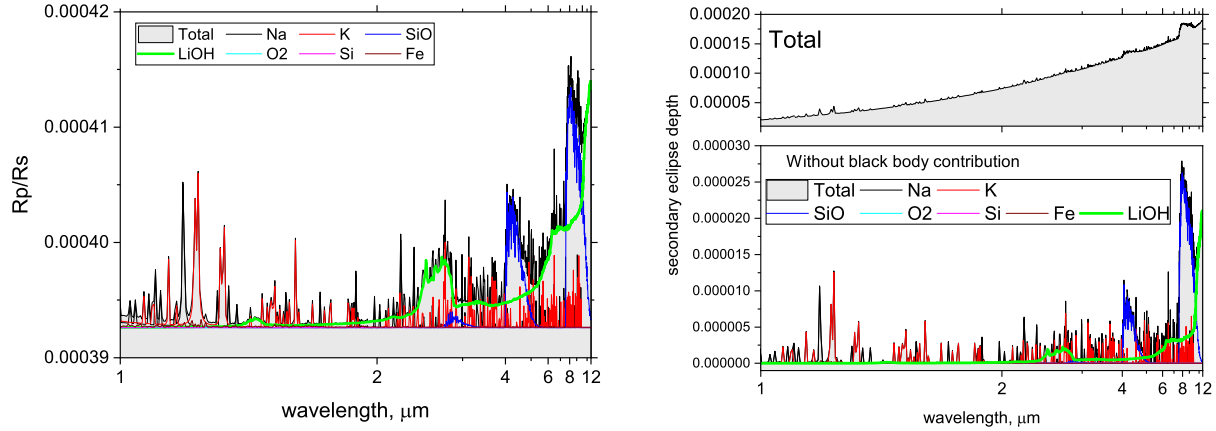

Figure 6. Detectable examples of LiOH in a 'mineral' exoplanetary atmosphere containing Na, K, SiO, O_2, Si, and Fe, where we added 0.001 part of LiOH (see Fig. 7). Left display: A transit spectrum (continous background) with all individual contributions shown using different lines with LiOH as a dark green colour. Right display: An emission (secondary eclipse) spectrum of a 'mineral' atmosphere (top panel); the lower panel is where the blackbody radiation background was subtracted and the main individual contributions are shown.

spin statistical weight $g_{ns} = 8$ for ^{7}LiOH. The pure rotational band of LiOH appears stronger in intensity than the rovibrationally excited bands when simulating absolute line intensities. However, simulating cross-sections at $T = 300$ K (lower panel of Fig. 3) changes this behaviour and the ν_2 bending mode becomes much stronger than the rotational band, in agreement with previous calculations of the dipole moments of these bands (Higgins et al. 2004).

The structure of the pure rotational band is shown in Fig. 4, where we have plotted absolute line intensities at $T = 300$ K against experimentally derived microwave data given by CDMS (Müller et al. 2001, 2005) based on the measurements of Higgins et al. (2004). There is good agreement between the strength of our line intensities with the CDMS values computed using a dipole moment value of 4.755 Debye (Higgins et al. 2004). Overall band shape is reproduced well, but our LiOH line list exhibits more structure as we have computed transitions up to $J = 95$. The lack of meaningful intensity information on the rovibrational bands of LiOH makes it difficult to quantify the accuracy of our line intensities. Past experience computing *ab initio* DMSs with similar levels of theory suggests that our LiOH transition intensities should be well within 5–10 per cent of experimentally determined values (Tennyson 2014; Yurchenko 2014).

To encourage future detection of LiOH in exoplanets, we have used the forward modelling capability of the TAUREX-III atmospheric modelling and retrieval code to generate example spectra with the rocky super-Earth 55 Cancri e as the example planet and the system parameters given in Ito et al. (2022). We have included the main isotopologue ^{7}Li^{16}O^{1}H on top of two base scenarios for the atmosphere: a water- and carbon dioxide-dominated case, and a mineral vapour-dominated case.

The strongest and most promising bands of LiOH in IR (2.6 μm) and near-IR (NIR; 1.35 μm) are from the O–H stretching mode, which unfortunately are masked by the H_2O bands. As an illustration, Fig. 5 shows a transit spectrum of an (exoplanetary) atmosphere consisting of 50/50 H_2O, CO_2 blend diluted down to introduce an example 5 per cent LiOH contribution, where CO_2 also partly overlaps with LiOH's 2.6 μm band. The NIR (6.7 μm) band of LiOH is formally in the window, but is probably too weak to make

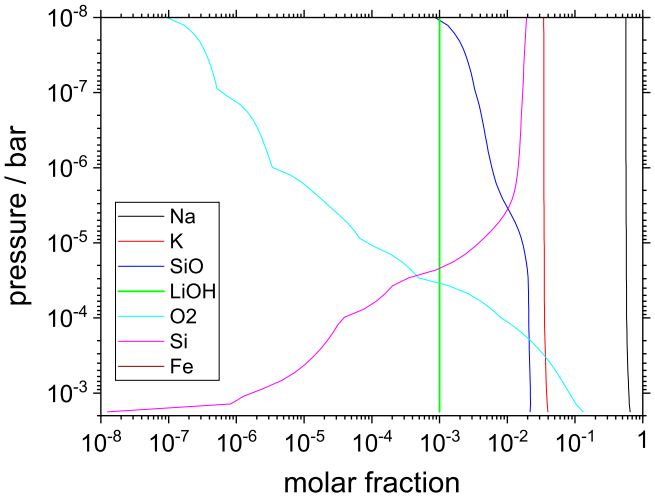

Figure 7. Composition of a 'mineral' atmosphere as *T*/*P* profiles of individual components based on Ito et al. (2022) with O omitted and LiOH included at an assumed constant value of 0.001.

a noticeable difference. The spectra have been produced with the radiative transfer code TAUREX-III (Al-Refaie et al. 2021) using the OYT7 LiOH opacities generated in this work, while the H_2O and CO_2 ExoMolOP opacities were produced using the corresponding ExoMol line lists (Polyansky et al. 2018; Yurchenko et al. 2020).

Fig. 6 shows a more optimistic scenario of detection, where we have added LiOH to a dayside-averaged, mineral-dominated atmosphere from Ito et al. (2022) containing Na, K, SiO, O_2, Si, and Fe, with neutral oxygen omitted in favour of an assumed 10^{-3} LiOH component (see composition in Fig. 7). The left display gives an example of a transit spectrum, while the right display shows an emission spectrum, where the lower part is with the blackbody radiation contribution subtracted for clarity. The underlying line lists are from HITRAN (Gordon et al. 2022) for O_2, ExoMol for SiO (Yurchenko et al. 2022), and Kurucz for the atomic lines (Kurucz 2011).

4 CONCLUSION

New line lists of lithium hydroxide ($^6Li^{16}O^1H$ and $^7Li^{16}O^1H$) covering wavelengths $\lambda > 1$ μm (0–10 000 cm^{-1}) have been presented. The OYT7 line lists were computed using the EVEREST nuclear motion code and are based on high-level *ab initio* potential energy and dipole moment surfaces. Transition wavenumbers and Einstein *A* coefficients were computed in the $\tilde{X}\,^1\Sigma^+$ ground electronic state for rovibrational states up to $J = 95$. The accuracy of the utilized PES was previously assessed (Koput 2013) and we expect line positions of the fundamental bands to be accurate to within 1 cm^{-1} on average, while line intensities should be accurate to within 5–10 per cent based on the chosen level of theory used to compute the DMS of LiOH. The strongest IR feature of LiOH corresponds to the ν_3 (O–H stretch) fundamental band at 2.6 μm, which might be difficult to detect in atmospheres of planets and stars due the fundamental band of H_2O in this region.

The usual ExoMol methodology is to utilize laboratory data to improve the accuracy of the computed line list (Tennyson 2012). However, the lack of gas-phase spectroscopic measurements of LiOH means that this has not been possible. If data become available in the future, then the line list will be updated. A number of purely *ab initio* line lists are available in the ExoMol database and they can greatly aid potential molecular detection. For example, a recent ExoMol *ab initio* line list of silicon dioxide (Owens et al. 2020) was used to show that SiO_2 would be a unique identifier of silicate atmospheres in lava world exoplanets (Zilinskas et al. 2022). It is hoped that the OYT7 line lists will assist future astronomical observations of LiOH. As well as the CaOH line list (Owens et al. 2022) mentioned above, the new OYT7 LiOH line list joins ones for NaOH and KOH already calculated as part of the ExoMol project (Owens, Tennyson & Yurchenko 2021).

ACKNOWLEDGEMENTS

We thank Yuichi Ito and Quentin Changeat for their help with the exoplanetary compositions. This work was supported by the STFC Projects ST/W000504/1. The authors acknowledge the use of the UCL Myriad High Performance Computing Facility and associated support services in the completion of this work, along with the Cambridge Service for Data Driven Discovery (CSD3), part of which is operated by the University of Cambridge Research Computing on behalf of the STFC DiRAC HPC Facility (www.dirac.ac.uk). The DiRAC component of CSD3 was funded by BEIS capital funding via STFC capital grants ST/P002307/1 and ST/R002452/1 and STFC operations grant ST/R00689X/1. DiRAC is part of the National e-Infrastructure. This work was also supported by the European Research Council (ERC) under the European Union's Horizon 2020 research and innovation programme through Advance Grant number 883830. YP's work has been carried out in the framework of the MSCA4Ukraine programme (Project Number: 1.4-UKR-1233448-MSCA4Ukraine). SOMW was supported by the STFC UCL Centre for Doctoral Training in Data Intensive Science (grant number ST/P006736/1). AO acknowledges additional support from the Engineering and Physical Sciences Research Council (grant number EP/S021582/1).

DATA AVAILABILITY

The states, transition, opacity, and partition function files for the LiOH line lists can be downloaded from www.exomol.com and the CDS data centre (cdsarc.u-strasbg.fr). The open access program EXOCROSS is available from github.com/exomol.

REFERENCES

Al-Refaie A. F., Changeat Q., Waldmann I. P., Tinetti G., 2021, ApJ, 917, 37
Bernath P. F., 2020, J. Quant. Spectrosc. Radiat. Transfer, 240, 106687
Birkby J. L., 2018, Handbook of Exoplanets. Springer, Cham, p. 1485
Bittner D. M., Bernath P. F., 2018, ApJS, 235, 8
Bunker P. R., Jensen P., Karpfen A., Lischka H., 1989, J. Mol. Spectrosc., 135, 89
Chubb K. L. et al., 2021, A&A, 646, A21
Császár A. G., Czakó G., Furtenbacher T., Mátyus E., 2007, Annu. Rep. Comput. Chem., 3, 155
D'Antona F., Mazzitelli I., 1998, in Rebolo R., Martin E. L., Zapatero Osorio M. R., eds, ASP Conf. Ser. Vol. 134, Brown Dwarfs and Extrasolar Planets. Astron. Soc. Pac., San Francisco, p. 442
Furtenbacher T., Császár A. G., 2012, J. Mol. Struct., 1009, 123
Furtenbacher T., Császár A. G., Tennyson J., 2007, J. Mol. Spectrosc., 245, 115
Gharib-Nezhad E., Marley M. S., Batalha N. E., Visscher C., Freedman R. S., Lupu R. E., 2021, ApJ, 919, 21
Gordon I. E. et al., 2022, J. Quant. Spectrosc. Radiat. Transfer, 277, 107949
Gurvich L. V., Bergman G. A., Gorokhov L. N., Iorish V. S., Leonidov V. Y., Yungman V. S., 1996, J. Phys. Chem. Ref. Data, 25, 1211

Higgins K. J., Freund S. M., Klemperer W., Apponi A. J., Ziurys L. M., 2004, J. Chem. Phys., 121, 11715
Hill C., Yurchenko S. N., Tennyson J., 2013, Icarus, 226, 1673
Irwin P. G. J. et al., 2008, J. Quant. Spectrosc. Radiat. Transfer, 109, 1136
Ito Y., Changeat Q., Edwards B., Al-Refaie A., Tinetti G., Ikoma M., 2022, Exp. Astron., 53, 357
Jørgensen U. G., Jensen P., 1993, J. Mol. Spectrosc., 161, 219
Kendall R. A., Dunning T. H., Harrison R. J., 1992, J. Chem. Phys., 96, 6796
Koput J., 2013, J. Chem. Phys., 138, 234301
Kurucz R. L., 2011, Can. J. Phys., 89, 417
Lodders K., Palme H., Gail H.-P., 2009, Landolt-Börnstein - Group VI Astronomy and Astrophysics, Volume 4B, Solar System. Springer-Verlag, Berlin, p. 712
Martín E. L., Lodieu N., del Burgo C., 2021, MNRAS, 510, 2841
McNaughton D., Tack L. M., Kleibömer B., Godfrey P. D., 1994, Struct. Chem., 5, 313
Min M., Ormel C. W., Chubb K., Helling C., Kawashima Y., 2020, A&A, 642, A28
Mitrushchenkov A. O., 2012, J. Chem. Phys., 136, 024108
Molliére P., Wardenier J. P., van Boekel R., Henning T., Molaverdikhani K., Snellen I. A. G., 2019, A&A, 627, A67
Müller H. S. P., Thorwirth S., Roth D. A., Winnewisser G., 2001, A&A, 370, L49
Müller H. S. P., Schlöder F., Stutzki J., Winnewisser G., 2005, J. Mol. Struct., 742, 215
Owens A., Yurchenko S. N., Yachmenev A., Tennyson J., Thiel W., 2015a, J. Chem. Phys., 142, 244306
Owens A., Yurchenko S. N., Yachmenev A., Thiel W., 2015b, J. Chem. Phys., 143, 244317
Owens A., Yurchenko S. N., Yachmenev A., Tennyson J., Thiel W., 2016, J. Chem. Phys., 145, 104305
Owens A., Conway E. K., Tennyson J., Yurchenko S. N., 2020, MNRAS, 495, 1927
Owens A., Tennyson J., Yurchenko S. N., 2021, MNRAS, 502, 1128
Owens A., Mitrushchenkov A., Yurchenko S. N., Tennyson J., 2022, MNRAS, 516, 3995
Pavlenko Y., 1997, Ap&SS, 253, 43
Pavlenko Y. V., Rebolo R., Martin E. L., Garcia Lopez R. J., 1995, A&A, 303, 807
Pavlenko Y., Zapatero Osorio M. R., Rebolo R., 2000, A&A, 355, 245
Polyansky O. L., Kyuberis A. A., Zobov N. F., Tennyson J., Yurchenko S. N., Lodi L., 2018, MNRAS, 480, 2597
Prascher B. P., Woon D. E., Peterson K. A., Dunning T. H., Wilson A. K., 2011, Theor. Chem. Acc., 128, 69
Rebolo R., Martin E. L., Magazzu A., 1992, ApJ, 389, L83
Rebolo R., Martin E. L., Basri G., Marcy G. W., Zapatero-Osorio M. R., 1996, ApJ, 469, L53
Ruiz M. T., Leggett S. K., Allard F., 1997, ApJ, 491, L107
Snellen I., 2014, Phil. Trans. R. Soc. A, 372, 20130075
Tennyson J., 2012, WIREs Comput. Mol. Sci., 2, 698
Tennyson J., 2014, J. Mol. Spectrosc., 298, 1
Tennyson J., 2016, J. Chem. Phys., 145, 120901
Tennyson J., Yurchenko S. N., 2012, MNRAS, 425, 21
Tennyson J., Yurchenko S. N., 2017, Int. J. Quantum Chem., 117, 92
Tennyson J. et al., 2016, J. Mol. Spectrosc., 327, 73
Tennyson J. et al., 2020, J. Quant. Spectrosc. Radiat. Transfer, 255, 107228
Tóbiás R., Furtenbacher T., Tennyson J., Császár A. G., 2019, Phys. Chem. Chem. Phys., 21, 3473
Tsuji T., 1973, A&A, 23, 411
Wang M., Audi G., Wapstra A., Kondev F., MacCormick M., Xu X., Pfeiffer B., 2012, Chin. Phys. C, 36, 1603
Watson J. K. G., 2003, J. Mol. Spectrosc., 219, 326
Werner H.-J., Knowles P. J., Knizia G., Manby F. R., Schütz M., 2012, WIREs Comput. Mol. Sci., 2, 242
Werner H.-J. et al., 2020, J. Chem. Phys., 152, 144107
Woon D. E., Dunning T. H., 1995, J. Chem. Phys., 103, 4572
Yurchenko S. N., 2014, Chemical Modelling: Volume 10. The Royal Society of Chemistry, London, p. 183
Yurchenko S. N., Al-Refaie A. F., Tennyson J., 2018, A&A, 614, A131
Yurchenko S. N., Mellor T. M., Freedman R. S., Tennyson J., 2020, MNRAS, 496, 5282
Yurchenko S. N. et al., 2022, MNRAS, 510, 903
Zapatero Osorio M. R., Béjar V. J. S., Pavlenko Y., Rebolo R., Allende Prieto C., Martín E. L., García López R. J., 2002, A&A, 384, 937
Zilinskas M., van Buchem C. P. A., Miguel Y., Louca A., Lupu R., Zieba S., van Westrenen W., 2022, A&A, 661, A126

SUPPORTING INFORMATION

Supplementary data are available at *MNRAS* online.

This includes the potential energy and dipole moment surfaces of LiOH with programs to construct them.
Please note: Oxford University Press is not responsible for the content or functionality of any supporting materials supplied by the authors. Any queries (other than missing material) should be directed to the corresponding author for the article.

This paper has been typeset from a TEX/LATEX file prepared by the author.